PAPER

Check for updates

Carbon-based artificial SEI layers for aqueous lithium-ion battery anodes†

Usha Subramanya,‡[a] Charleston Chua,‡[a] Victor Gin He Leong,[a] Ryan Robinson,[a] Gwenlyn Angel Cruz Cabiltes,[a] Prakirti Singh,[a] Bonnie Yip,[a] Anuja Bokare,[b] Folarin Erogbogbo[b] and Dahyun Oh [ID] *[a]

Replacing flammable organic electrolytes with aqueous electrolytes in lithium-ion batteries (LIB) can greatly enhance the safety of next-generation energy storage systems. With the extended electrochemical stability window of electrolytes, 'water-in-salt' (WIS) electrolytes containing LIB presented significant performance improvements. However, the solubility limits of lithium salts in water restrain the extent of kinetic protection offered by the high salt concentration. Here, we report design strategies of anode structure to improve the cycle life of LIB with WIS electrolytes. We introduced partially graphitic protective carbon layers on anode particles using a versatile coating method. This protective layer not only improved charge transfer kinetics but also minimized the exposure of anode surface for water electrolysis. The effectiveness of anode structure developed in this study was exemplified on TiO_2 anodes, where cycle performance and coulombic efficiency improved by 11 times and 29% respectively over the base anode material.

1. Introduction

Developing safe and cost-effective batteries has become an important issue in scientific communities due to the high demand for storing electricity for mobile devices and electric vehicles. Currently, lithium-ion batteries (LIB) use highly flammable and toxic organic electrolytes that can lead to explosions. Aqueous LIB can address this safety issue by replacing flammable organic electrolytes.[1–3] However, their poor cycle life and low energy density hinder their greater adoption in consumer products such as mobile electronics or electric vehicles. These issues stem from the narrow electrochemical stability window of water (1.23 V),[2] limiting the selection of active materials that can stably operate within this potential range.[4–7] This has not been an issue in organic electrolytes because of the formation of stable solid-electrolyte interphase (SEI) layers. These layers were known to be formed by the deposition of electrolyte decomposition products and prevent further degradation of electrolytes.[8–12] However, aqueous electrolyte decomposition products like oxygen and hydrogen gas cannot form surface layers on electrode surfaces.[1,13] Recent studies have shown that the use of a highly concentrated 'water-

in-salt' (WIS) electrolyte results in preferential decomposition of lithium salts, forming SEI layers on the anode primarily consisting of LiF.[14] This extends the electrochemical stability window of aqueous electrolytes from 1.23 V to 3.00 V, as the interphase layer suppresses further electrolyte decomposition.[2,15,16]

While highly-concentrated aqueous electrolytes extend the stability window of aqueous batteries to 3 V, their cyclability and energy density are still inferior to organic electrolytes-based batteries.[6,13,17] Thus, an alternative solution to achieve performance parity needs to be developed to overcome limitations arising from the solubility limit of salt in water and high cost of lithium salts in super-concentrated electrolytes. To that end, we propose to develop a design strategy for a protective layer on anode particles analogous to SEI layers to minimize battery performance degradation in aqueous LIB. Due to its high electronic conductivity and easy formation on diverse substrates, carbon-based protective layer has been widely used to improve the electrode performance in organic electrolyte.[18,19] However, this has not been widely explored in 'water-in-salt' electrolyte batteries. Carbon–water interactions necessitate a balance between 'graphitic' and 'amorphous' bonding due to differing hydrophobicity and conductivity. Here we systematically determine and report the key parameters to develop an ideal carbon coating on anode as a form of artificial SEI layer (Fig. 1A) for aqueous LIB. We aim to build nanometer thick protective layers on anode particles that provide diffusion channels for lithium ions while minimizing the access of water molecules to electrode surfaces.

[a]Chemical and Materials Engineering Department, Charles W. Davidson College of Engineering, San José State University, One Washington Square, San José, CA 95192-0080, USA. E-mail: dahyun.oh@sjsu.edu

[b]Biomedical Engineering Department, Charles W. Davidson College of Engineering, San José State University, One Washington Square, San José, CA 95192-0080, USA
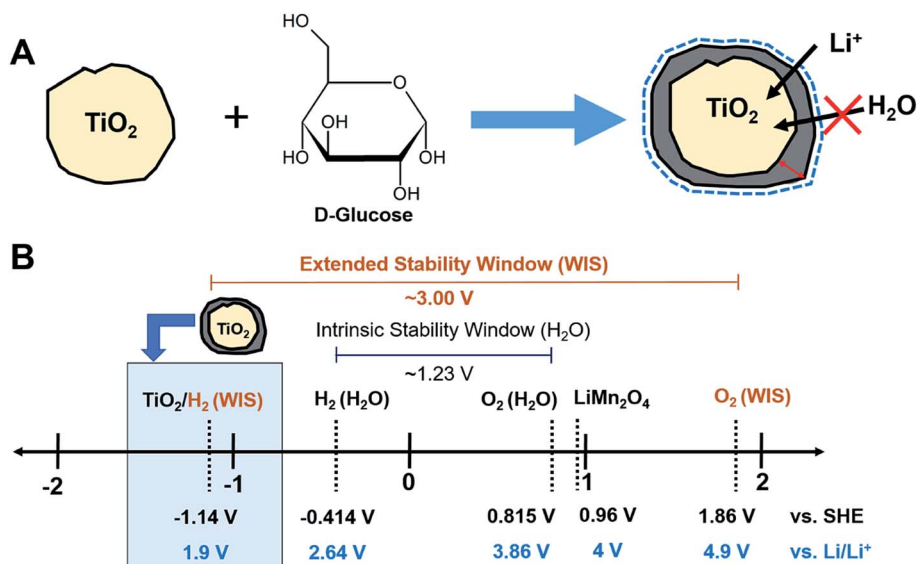
‡ These authors contributed equally.

Fig. 1 Schematics of (A) carbon coating process and (B) the stability window of water-in-salt (WIS) electrolyte with the electrochemical redox potentials of battery cell components in this study (anode: TiO_2 and cathode: $LiMn_2O_4$).

To exemplify the effectiveness of our artificially created SEI layer, we chose titanium dioxide (TiO_2) as our model anode material (Fig. 1B). TiO_2 presented low volumetric expansion during lithium intercalation in LIB with organic electrolytes, resulting in a good cycle life.[20,21] Several polymorphs of TiO_2 exist including anatase, bronze (TiO_2-B), rutile, *etc.*, each of which has shown different electrochemical reactions with lithium ions.[22] For battery applications, the anatase phase is preferred as it is a thermodynamically stable phase and showed superior electrochemical performance to the majority of the other phases with good insertion kinetics (0.5 Li per formula unit).[23–26] While TiO_2 itself is stable in aqueous electrolyte batteries, due to its photocatalytic properties and close operating potential to hydrogen evolution, continual water decomposition can possibly occur on its surface without protective layers. Therefore, this work investigates the optimal thickness and composition of carbon needed to improve the performance of TiO_2 anodes in aqueous LIB. By using glucose, an inexpensive common precursor, we developed a diverse range of artificial SEI layers on anodes to reduce the anode surface area available for water electrolysis and to improve the conductivity of anodes (Fig. 1A). Our findings presented synthesis guidelines for creating an artificial SEI layer designed to improve the aqueous LIB performance. This general anode design strategy to improve the aqueous battery performance can provide safer and higher performing next-generation aqueous LIB that can transform the current energy storage paradigm in a more sustainable manner.

2. Experimental section

Anatase TiO_2 nanoparticles were synthesized using a sol–gel synthesis process. First, 8 mL of titanium isopropoxide (≥97%, Aldrich, called as TTIP in this work) was added into 33 mL of ethanol (>99.5%, Acros Organics) slowly while stirring. Four

drops of nitric acid (>99%, Aldrich) were then added into the solution and stirred for 10 minutes. Deionized water was added dropwise for 2 min (3 mL) into this solution and a gel was formed. The resulting gel was aged for 24 hours at room temperature, then heated under vacuum for 48 hours at 95 °C. The dried products were ground into fine powder and annealed at 500 °C for 3 hours in a furnace.[27] Coating of the sol–gel TiO_2 (named as C-TiO_2) was done using a carbothermal synthesis method. Different weight ratios of TiO_2 and glucose (1 : 2, 1 : 4, 1 : 6, 1 : 9 = TiO_2 : glucose) were mixed in 17.5 mL of deionized water for 45 minutes using a bath sonicator and then stirred for 3 hours on a magnetic stirring plate. The solution was then heated at 180 °C in a 23 mL Teflon-lined stainless-steel autoclave for 12 hours. The resulting brown mixture was washed with deionized water by centrifugation until the solution became clear.[28,29] The solution was then dried at 80 °C in a vacuum oven for 6 hours followed by annealing in a tube furnace under Ar at varying temperatures (400–900 °C).

Anodes were fabricated with 8 : 1 : 1 mass ratio mixture of TiO_2 powder, carbon black (Super P®, Alfa Aesar), and poly(tetrafluoroethylene) (Sigma Aldrich). The electrodes were punched using a 3/8″ diameter hole punch. To indemnify the irreversible loss of cyclable lithium, the mass of the cathode was maintained at twice of the mass of the anode. The weight of anode was around 10 mg cm^{-2}. The batteries were fabricated using a WIS electrolyte and $LiMn_2O_4$ cathode (MTI corporation, Al foil single side coated). The water-in-salt electrolyte was prepared by mixing 21 m (molality, mol kg^{-1}) of lithium bis(trifluoromethanesulfonyl)imide (Gotion) in deionized water at 50 °C for 1 hour followed by continuous stirring at room temperature for 24 hours. The coin cells (CR2032) were assembled by placing the anode on the bottom cap of the cell followed by a glass microfiber separator (Whatman grade GF/A, 1.6 μm), 200 μL of WIS electrolyte, and cathode.

Galvanostatic measurements were done using the battery analyzer (MTI Corporation, BST8-WA) at a 0.2 or 0.5C rate for a voltage range of 0.8 V to 2.5 V at room temperature. Electrochemical impedance spectroscopy was done at OCV using an impedance analyzer (Gamry 1010E) using a frequency range of 0.01 Hz to 0.5 MHz with 10 mV of AC voltage. Before measurement, all battery samples were rested for a minimum of 5 hours. To determine the impedance contribution from individual electrode components, a symmetric cell approach was taken for impedance characterization, where a pair of coin cells were charged to a 100% state-of-charge (SOC) followed by storage at room temperature for a minimum of 4 days. After storage, each cell was opened and the anode of one cell was swapped with the cathode of the other to create two symmetric cells as shown in the ESI.†

X-ray diffraction (XRD) patterns were collected using a Rigaku Ultima III with Cu source (accelerating voltage and current of 40 kV and 44 mA) with a $1.5°$ min^{-1} of scan speed and a range taken as $2\theta = 20–80°$. Raman spectra were obtained using a Horiba LabRam Aramis Confocal Microscope with a 532 nm excitation laser and a $50\times$ LWD objective lens. The spot size was 1–2 μm with power density of 0.64–2.6 mW μm^{-2}. Transmission electron microscopy (TEM) images were collected using a JEOL 3010 electron microscope at an accelerating voltage of 300 kV. The thermogravimetric analyses (TGA, TA Instruments 5500) of the sol–gel TiO_2 and $C-TiO_2$ were done using 10 °C min^{-1} of heating rate under air.

3. Results/discussion

TiO_2 was commonly used as a photoanode for photoelectrochemical water splitting[30–33] and has low conductivity due to its wide bandgap (3.2 eV).[34] To overcome these drawbacks for battery applications, an artificial SEI layer of carbon was introduced onto the TiO_2 surface. The carbon coating prevents a direct electrochemical contact between the anode and water molecule thereby minimizing water electrolysis. We controlled the properties of this carbon layer by adjusting two key parameters, (1) the annealing temperature and (2) the mass ratio of active material to carbon precursor. The mass ratio of active material and glucose precursor determined the amount of carbon in $C-TiO_2$ and the annealing temperature changed the amount of graphitic carbon as well as the conductivity. The annealing temperature must be carefully chosen because of the possibility of TiO_2 phase transformation from anatase to rutile.

We first determined the ideal range of annealing temperature of $C-TiO_2$ by investigating the evolution of crystal phase using XRD (Fig. 2A). Only the annealing temperature was varied while keeping the ratio of TiO_2 to glucose constant at 1 : 4 to find appropriate annealing temperature windows for $C-TiO_2$ synthesis. Because anatase TiO_2 showed a better lithium storage capacity than rutile TiO_2,[35] we aimed to preserve anatase phase during the carbon coating process. As some degree of phase transformation from anatase to rutile was observed in XRD after annealing $C-TiO_2$ at 900 °C, annealing temperature below 900 °C was set as a limit of the $C-TiO_2$ synthesis process in this study. Crystal sizes (Table 1) did not appreciably change within

this annealing temperature range (400–900 °C), that could originate from the constrained growth due to the carbon coating.[28] This provides a good similarity of TiO_2 used for different coating conditions enabling us to evaluate the effect of carbon layer on aqueous LIB performance.

The amount of the carbon shell present in $C-TiO_2$ needs to be sufficient enough to enhance the conductivity of the battery electrode but also needs to be as small as possible to lower the diffusion barrier for lithium-ions to reach active materials. To develop an ideal composition of $C-TiO_2$ for aqueous LIB, we varied mass ratios of TiO_2 to glucose as 1 : 2, 1 : 4, 1 : 6, and 1 : 9 during the synthesis. The amounts of carbon in $C-TiO_2$ synthesized with different ratios of glucose precursor to TiO_2 were determined by TGA. TGA plots presented two plateaus for all different compositions of $C-TiO_2$ (Fig. S1†), with the first plateau starting around 100 °C and the second plateau starting around 400 °C. At the first plateau, a total weight loss of around 2% was observed, corresponding to the evaporation of physically absorbed water. The second plateau (350–400 °C) is expected to originate from the carbon decomposition in $C-TiO_2$. This second plateau is lower than the decomposition temperature of graphite[36,37] possibly due to the incomplete graphitization of carbon in $C-TiO_2$. In summary, the weight percentages of carbon in $C-TiO_2$ composites were around 10, 18, 50, and 70% for $C-TiO_2$ composites synthesized with 1 : 2, 1 : 4, 1 : 6, and 1 : 9 of precursor ratios (Fig. 2B).

The electrochemical performances of $C-TiO_2$ anodes with different carbon amounts were investigated in aqueous LIB (Fig. 3). Fig. 3A shows the 1st and 40th cycling voltage profiles of aqueous LIB with sol–gel TiO_2 or $C-TiO_2$ anodes (fabricated with 1 : 2, 1 : 4, 1 : 6, and 1 : 9 of precursor ratios) tested against $LiMn_2O_4$ cathodes with 21 m LiTFSI aqueous electrolyte at 0.2C rates. During the first charging step, some irreversible loss of charges might be associated with the SEI layer formation on the surface of anode.[12] As discussed earlier, this SEI layer acts as a passivation layer and blocks direct contact between electrode and water molecules, preventing further electrolyte decomposition. This irreversible capacity loss due to the SEI formation presented lower coulombic efficiencies for the initial 10 cycles for all compositions of anodes (Fig. 3C). Among $C-TiO_2$ anodes fabricated with different weight fractions of carbon, $C-TiO_2$ anodes made with 1 : 4 of precursor ratio showed better improvements in cycle life and coulomb efficiency than other $C-TiO_2$ anodes. Having the carbon layer on anodes lowered the initial capacity, however, $C-TiO_2$ anodes showed a better capacity retention in the following cycles than that of the battery tested with sol–gel TiO_2 anodes (Fig. 3A and B). $C-TiO_2$ anodes with higher carbon ratios (1 : 6 and 1 : 9) showed a lower coulombic efficiency than lower ratios (1 : 2 and 1 : 4) at 40th cycle. This may be attributed to the loss of lithium ions in thick interlayers made of large amounts of carbon precursors. Although the first discharge capacity of sol–gel TiO_2 was higher than that of $C-TiO_2$ with 1 : 4 ratio, $C-TiO_2$ anodes with 1 : 4 ratio showed almost four times higher capacity at the end of 40th cycle than that of sol–gel TiO_2. This suggests that 1 : 4 ratio is optimal to form stable SEI layers for aqueous LIB.
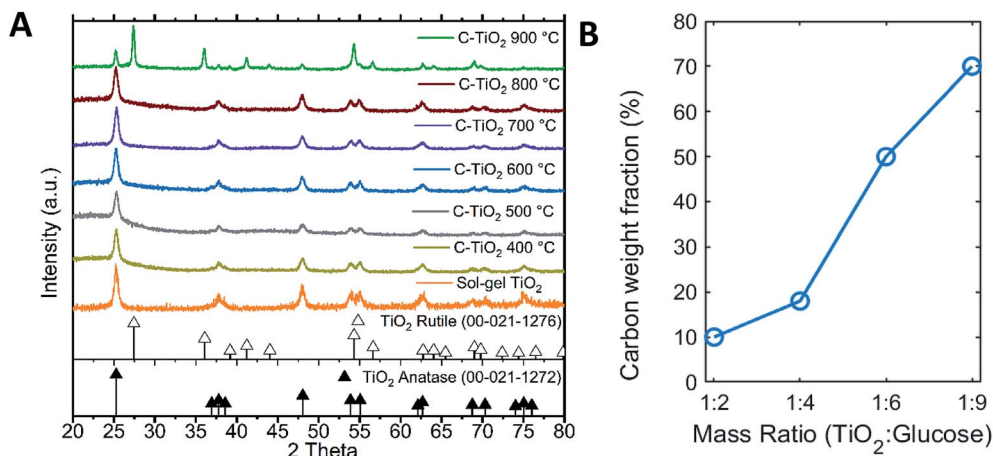
Fig. 2 The material properties of carbon coated TiO_2 (C-TiO_2). (A) XRD patterns of C-TiO_2 measured with a scan speed of 1.5° min^{-1} for a range of $2\theta = 20-80°$. (B) The weight fractions of carbon in C-TiO_2 synthesized with varied precursor ratios of TiO_2 to glucose mixture using TGA with a heating rate of 10 °C min^{-1} under air.

To investigate the influence of graphitic layer of C-TiO_2 nanoparticles on aqueous LIB performance, the annealing temperatures were adjusted to control the fraction of graphitic carbon in C-TiO_2 nanoparticles. The carbon amount in C-TiO_2 was fixed the same as 18% or 70% (prepared with the precursor ratio of 1 : 4 and 1 : 9, respectively), and the annealing temperature was varied from 400 °C to 600 °C. The carbon layer distribution and its composition were investigated using TEM and Raman spectroscopy. While a clean edge of TiO_2 crystal was observed for the TiO_2 samples without carbon coatings (Fig. 4A), around 2–5 nm thick carbon layers were surrounding TiO_2 crystals in C-TiO_2 nanoparticles as can be seen in Fig. 4B. Using the Raman spectra of C-TiO_2 nanoparticles, the effect of carbon layer annealing temperature on graphitization was studied. First, we observed the signature peak of TiO_2 (E_g, A_{1g}, and B_{1g} peaks) in the Raman spectra of C-TiO_2 confirming the presence of anatase TiO_2 nanoparticles (Fig. S2†).[38,39] The D and G peaks were found at ~1360 cm^{-1} and ~1560 cm^{-1} in the Raman spectra of C-TiO_2 (Fig. 4C), with a noticeable absence of the second order D peak.[40] This is characteristic of amorphous carbons with little to no long range order, consistent with literature using this carbon coating process.[28] The effects of

annealing temperature on the composition of the carbon coating were further analyzed using the D peak intensity divided by the G peak intensity. The G peak is associated with graphitic in-plane vibrations with E_{2g} symmetry, while the D peak is associated with defective graphite.[11] As such the I_D/I_G parameter is commonly used to characterize disorder in a carbon sample. Given that graphitic carbon has greater conductivity than amorphous carbon, it is desirable to minimize I_D/I_G to further improve the conductivity of the carbon layer. Using Fig. 4D, there is a clear tendency towards decreasing I_D/I_G as the heat treatment temperature of the coating process increases from 400 °C to 600 °C for both C-TiO_2 samples prepared with 1 : 4 and 1 : 9 precursor ratios.

The variation in disorder of carbon layer had a significant influence on the aqueous LIB performance (Fig. 5). Annealing C-TiO_2 at 600 °C was the most effective to improve the cycle performance compared to 400 °C, 800 °C or 900 °C (Fig. 5A, B and S3†). The first cycle coulombic efficiency of anodes with C-TiO_2 annealed at 400 °C was similar to that of C-TiO_2 annealed at 600 °C. However, the first discharge capacity of C-TiO_2 annealed at 400 °C was only 60 mA h g^{-1} while C-TiO_2 annealed at 600 °C showed about ~35% higher first discharge capacity.

Table 1 Crystal phases and lattice parameters of sol–gel TiO_2 and C-TiO_2 annealed at different temperatures

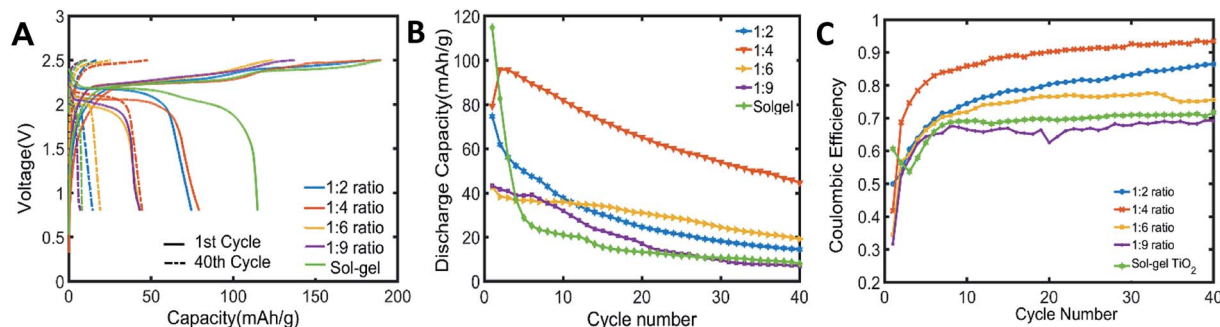| Material	Annealing temperature	Phase	Crystalline size (Å)	Lattice parameters (Å)		
				a	b	c
Sol–gel TiO_2	400	Anatase	130	3.787	3.789	9.505
C-TiO_2	400	Anatase	161	3.789	3.789	9.505
	500	Anatase	142	3.787	3.787	9.505
	600	Anatase	137	3.784	3.784	9.498
	700	Anatase	145	3.793	3.793	9.516
	800	Anatase	154	3.788	3.788	9.501
	900	Rutile (69%)	>1000	4.593	4.593	2.958
		Anatase (31%)	>814	3.785	3.785	9.509

Fig. 3 The aqueous LIB performance of C-TiO$_2$ anodes with varied amounts of carbon shell in C-TiO$_2$. The batteries were tested with WIS electrolyte (21 m LiTFSI in H$_2$O) and LiMn$_2$O$_4$ cathode at C/5. The carbon layer on C-TiO$_2$ was formed by annealing at 600 °C. (A) Voltage profiles of aqueous batteries at the 1st and 40th cycle with anodes made of sol–gel TiO$_2$ or C-TiO$_2$ synthesized with different weight fractions of precursors (1 : 2, 1 : 4, 1 : 6 and 1 : 9). (B) Cycling performances of aqueous LIB with sol–gel TiO$_2$ anodes or C-TiO$_2$ anodes fabricated with different mass ratios and corresponding (C) coulombic efficiencies.

The irreversible capacity loss during the initial cycles is associated with the formation of SEI, thus, C-TiO$_2$ annealed at 400 °C did not form a stable SEI layer as can be seen from its lower coulombic efficiencies than that of 600 °C. Coulombic efficiencies of C-TiO$_2$ anodes treated at 600 °C were maintained higher than that of 400 °C until 40th cycle (Fig. 5C), indicating a stable formation of SEI in aqueous LIB. We also expect that the carbon layer's increased conductivity might improve the battery performance compared to the C-TiO$_2$ nanoparticles treated at 400 °C. However, further increasing the temperature to 900 °C resulted in the phase transformation of anatase TiO$_2$ nanoparticles degrading the battery performance due to inferior electrochemical activity of rutile compared to anatase (Fig. S3†).[23] Therefore, it is suggested to treat the C-TiO$_2$ composite below 900 °C to maximize its aqueous LIB performance. In previous works, LiF, Li$_2$O, LiOH, and Li$_2$CO$_3$ were observed on the anode surface in WIS based LIB after cycling.[14,41] These are the main components comprising the SEI layer with WIS electrolytes. The defective carbon layer made by a hydrothermal carbonization process of carbohydrate could be a good source of precursor for Li$_2$O, LiOH, and Li$_2$CO$_3$ formation. How the defective carbon layer and TFSI anions coordinate to produce LiF or the detail analysis of interface in WIS based LIB would require *in situ* analysis that remains as our future study.

To better understand the effect of the artificial SEI on battery degradation, electrochemical impedance spectroscopy was used to characterize the surface layer and charge transfer impedance evolution over cycling as shown in Fig. 6. The equivalent circuit model used for fitting our system is shown in the inset of Fig. 6A, where R_S and R_{CT} are associated with resistances arising from surface layer formation and charge transfer of the anode material, respectively. We assigned these resistances to the anode based on the result from the symmetric cell approach, which shows that impedance from the cathode does not contribute greatly over cycling as shown in Fig. S4.† Typically, R_S and R_{CT} are associated with the high (>10 kHz) and medium (0.16–630 Hz) frequency semicircles[42–44] and we applied a model that fits the high and medium frequency regions well.[45] Overall, the carbon coating on anodes greatly reduced impedance evolution over cycling. The cycled electrodes were also investigated with SEM and XRD but no significant changes were observed (Fig. S5†). The surface layer impedance at 100 cycles for uncoated and coated TiO$_2$ are 101 and 27.61 ohms, respectively, and the charge transfer resistances for uncoated and coated TiO$_2$ are 982.2 and 167.6 ohms respectively, as summarized in Table 2. The decreased R_S and R_{CT} of C-TiO$_2$ are attributed to the carbon coating that we applied on TiO$_2$. For coated TiO$_2$ anodes, R_S did not greatly increase over cycling because carbon layers are expected to inhibit further growth of
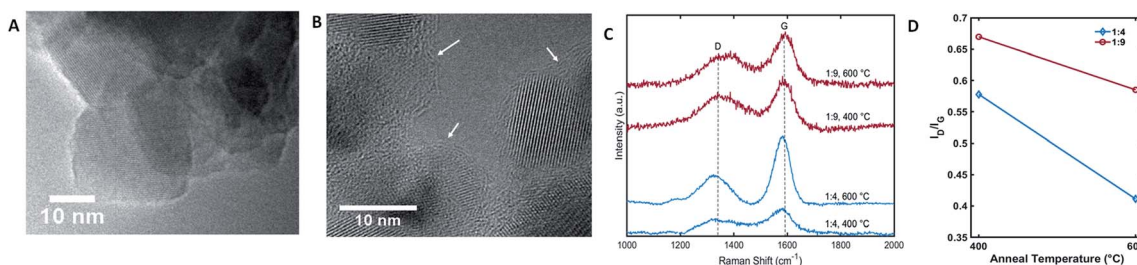

Fig. 4 The properties of carbon layer on C-TiO$_2$. TEM images (A) sol–gel TiO$_2$ and (B) C-TiO$_2$ with 1 : 4 of precursor ratio and annealed at 600 °C. Crystalline lattices corresponding to anatase TiO$_2$ were observed in both (A) and (B). The arrows in (B) indicate the carbon layer surrounding TiO$_2$ particles. Raman spectra (C) of C-TiO$_2$ synthesized with different precursor ratios of TiO$_2$: glucose and annealing temperatures. The intensities of I_D and I_G were compared by calculating I_D/I_G ratio (D) of C-TiO$_2$ synthesized with different mass ratios and annealing temperatures.
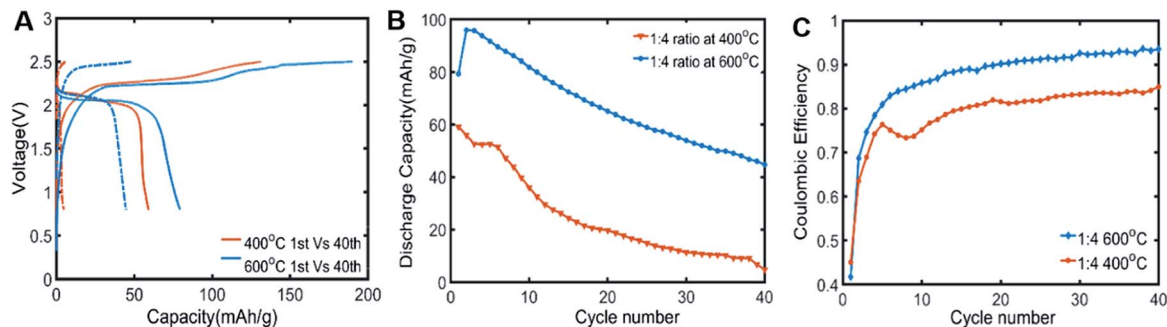
Paper

RSC Advances

Fig. 5 The full cell performance of C–TiO$_2$ anodes with different annealing temperature of carbon layer. The precursor ratio for C–TiO$_2$ synthesis was fixed as 1 : 4 (TiO$_2$: glucose). (A) Voltage profiles of aqueous batteries at the 1st and 40th cycle tested with C–TiO$_2$ anodes annealed at 400 °C and 600 °C. (B) Cycling performance and (C) corresponding coulombic efficiency of C–TiO$_2$ anodes annealed at 400 °C and 600 °C.
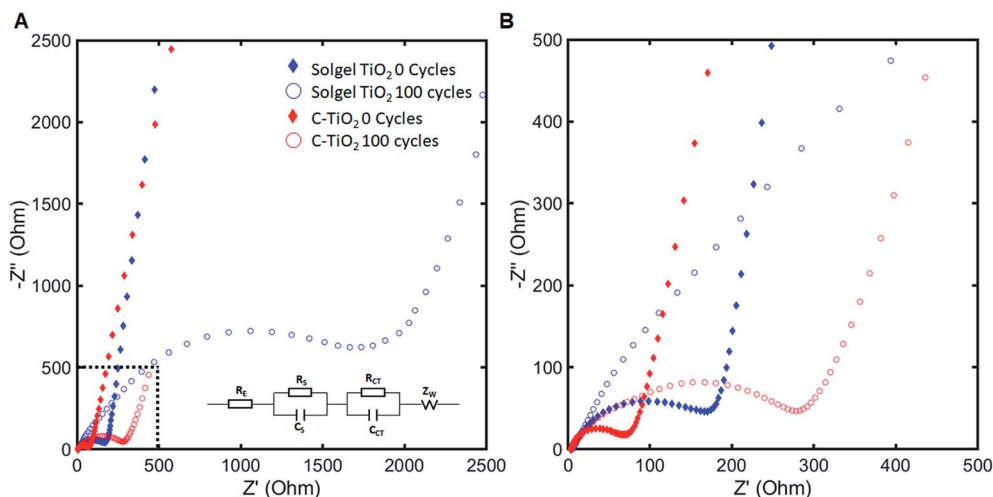

Fig. 6 Impedance analysis of aqueous batteries with sol–gel TiO$_2$ anodes and C–TiO$_2$ anodes (1 : 4 of precursor ratio and annealed at 600 °C). (A) Nyquist plots of coated (C–TiO$_2$) and uncoated (sol–gel TiO$_2$) batteries for 0 and 100 cycles and proposed model (inset). (B) High and middle frequency regions of Nyquist plot in (A).

**Table 2** Fitted values of resistances (R_S, R_{CT}) using the model in Fig. 6A

Material	Initial R_S (ohm)	100 cycle R_S (ohm)	Initial R_{CT} (ohm)	100 cycle R_{CT} (ohm)
Sol–gel TiO$_2$	0	101.0	78.23	982.2
C–TiO$_2$, 600 °C	38.08	27.61	1.048	167.6

surface layer from electrolyte decomposition as it can be also supported by improved coulombic efficiencies. In addition, improved conductivity of anode particles with carbon layer might enhance the charge transfer during the battery reaction, thus enhancing overall battery performances.

4. Conclusion

In summary, the effect of carbon coating on anodes on aqueous LIB performance was investigated. Using a versatile carbon coating method, TiO$_2$ nanoparticles were encapsulated, improving cycle performance and coulombic efficiency of the anode by 11 times and 29% respectively over sol–gel TiO$_2$ anodes. We attribute these improvements to: (1) the conductive carbon layer, reducing charge transfer resistance and (2) the reduced contact between the water molecules and the anode, lowering the rate of electrolyte decomposition. Our findings show that 18 wt% of carbon fractions to encapsulate TiO$_2$ is ideal to improve aqueous LIB performance. At this synthesis condition, the thickness of the carbon layer was sufficient to inhibit the electrolyte decomposition while allowing the charge transfer. We also found a calcination temperature of 600 °C to be ideal as the conductivity of the carbon layer was maximized while maintaining the anatase phase of the TiO$_2$. To further
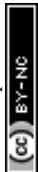
enhance the energy storage capability of aqueous LIB, selecting anode materials with higher theoretical capacity and lower redox potential than TiO_2 would be essential. For carbon-based artificial SEI, we found that the thickness and composition of carbon play a critical role in battery performance. Our findings suggest that controlling the property of the nanometer thick protective layer can greatly enhance the battery performance and an effective artificial SEI layer would enable us to develop safe and long-lasting next-generation aqueous LIB.

Author contributions

U. S. and C. C. performed and designed the experiment. V. L, R. R. and A. B. synthesized sol–gel TiO_2. G. A. C. C and P. S. performed carbon coating experiment. B. Y. and C. C. performed the impedance analysis. F. E. supervised the synthesis process of sol–gel TiO_2. D. O. supervised the project. All authors have given approval to the final version of the manuscript.

Funding sources

Conflicts of interest

There are no conflicts to declare.

Acknowledgements

References

1 W. Li, J. R. Dahn and D. S. Wainwright, *Science*, 1994, **264**, 1115–1118.
2 J.-Y. Luo, W.-J. Cui, P. He and Y.-Y. Xia, *Nat. Chem.*, 2010, **2**, 760–765.
3 J. M. Tarascon and M. Armand, *Nature*, 2001, **414**, 359–367.
4 C. Yang, J. Chen, T. Qing, X. Fan, W. Sun, A. von Cresce, M. S. Ding, O. Borodin, J. Vatamanu, M. A. Schroeder, N. Eidson, C. Wang and K. Xu, *Joule*, 2017, **1**, 122–132.
5 B. Scrosati, J. Hassoun and Y.-K. Sun, *Energy Environ. Sci.*, 2011, **4**, 3287–3295.
6 Y. Wang, J. Yi and Y. Xia, *Adv. Energy Mater.*, 2012, **2**, 830–840.
7 W. Li, W. R. McKinnon and J. R. Dahn, *J. Electrochem. Soc.*, 1994, **141**, 2310–2316.
8 H. Buqa, A. Würsig, J. Vetter, M. E. Spahr, F. Krumeich and P. Novák, *J. Power Sources*, 2006, **153**, 385–390.
9 K. Xu, *Chem. Rev.*, 2014, **114**, 11503–11618.
10 E. Peled and S. Menkin, *J. Electrochem. Soc.*, 2017, **164**, A1703–A1719.
11 S. J. An, J. Li, C. Daniel, D. Mohanty, S. Nagpure and D. L. Wood, *Carbon*, 2016, **105**, 52–76.
12 X. Yu and A. Manthiram, *Energy Environ. Sci.*, 2018, **11**, 527–543.
13 H. Kim, J. Hong, K.-Y. Park, H. Kim, S.-W. Kim and K. Kang, *Chem. Rev.*, 2014, **114**, 11788–11827.
14 L. Suo, D. Oh, Y. Lin, Z. Zhuo, O. Borodin, T. Gao, F. Wang, A. Kushima, Z. Wang, H.-C. Kim, Y. Qi, W. Yang, F. Pan, J. Li, K. Xu and C. Wang, *J. Am. Chem. Soc.*, 2017, **139**, 18670–18680.
15 L. Suo, O. Borodin, W. Sun, X. Fan, C. Yang, F. Wang, T. Gao, Z. Ma, M. Schroeder, A. von Cresce, S. M. Russell, M. Armand, A. Angell, K. Xu and C. Wang, *Angew. Chem., Int. Ed.*, 2016, **55**, 7136–7141.
16 C. Yang, L. Suo, O. Borodin, F. Wang, W. Sun, T. Gao, X. Fan, S. Hou, Z. Ma, K. Amine, K. Xu and C. Wang, *Proc. Natl. Acad. Sci. U. S. A.*, 2017, **114**, 6197–6202.
17 L. Suo, O. Borodin, T. Gao, M. Olguin, J. Ho, X. Fan, C. Luo, C. Wang and K. Xu, *Science*, 2015, **350**, 938–943.
18 H. Liu, W. Li, D. Shen, D. Zhao and G. Wang, *J. Am. Chem. Soc.*, 2015, **137**, 13161–13166.
19 G. Wang, H. Liu, J. Liu, S. Qiao, G. M. Lu, P. Munroe and H. Ahn, *Adv. Mater.*, 2010, **22**, 4944–4948.
20 M. Madian, A. Eychmüller and L. Giebeler, *Batteries*, 2018, **4**, 7.
21 H. Lahan, R. Boruah, A. Hazarika and S. K. Das, *J. Phys. Chem. C*, 2017, **121**, 26241–26249.
22 S. M. Gupta and M. Tripathi, *Chin. Sci. Bull.*, 2011, **56**, 1639.
23 S. S. El-Deen, A. M. Hashem, A. E. Abdel Ghany, S. Indris, H. Ehrenberg, A. Mauger and C. M. Julien, *Ionics*, 2018, **24**, 2925–2934.
24 D. W. Murphy, R. J. Cava, S. M. Zahurak and A. Santoro, *Solid State Ionics*, 1983, **9–10**, 413–417.
25 I. Issac, M. Scheuermann, S. M. Becker, E. G. Bardají, C. Adelhelm, D. Wang, C. Kübel and S. Indris, *J. Power Sources*, 2011, **196**, 9689–9695.
26 D. Su, S. Dou and G. Wang, *Chem. Mater.*, 2015, **27**, 6022–6029.
27 A. Bokare, M. Pai and A. A. Athawale, *Sol. Energy*, 2013, **91**, 111–119.
28 L.-W. Zhang, H.-B. Fu and Y.-F. Zhu, *Adv. Funct. Mater.*, 2008, **18**, 2180–2189.
29 M. T. García-Valverde, R. Lucena, F. Galán-Cano, S. Cárdenas and M. Valcárcel, *J. Chromatogr. A*, 2014, **1343**, 26–32.
30 A. Fujishima and K. Honda, *Nature*, 1972, **238**, 37–38.
31 J. H. Park, S. Kim and A. J. Bard, *Nano Lett.*, 2006, **6**, 24–28.
32 A. J. Cowan, J. Tang, W. Leng, J. R. Durrant and D. R. Klug, *J. Phys. Chem. C*, 2010, **114**, 4208–4214.
33 Z.-W. Yin, S. B. Betzler, T. Sheng, Q. Zhang, X. Peng, J. Shangguan, K. C. Bustillo, J.-T. Li, S.-G. Sun and H. Zheng, *Nano Energy*, 2019, **62**, 507–512.

34 C. Dette, M. A. Pérez-Osorio, C. S. Kley, P. Punke, C. E. Patrick, P. Jacobson, F. Giustino, S. J. Jung and K. Kern, *Nano Lett.*, 2014, **14**, 6533–6538.

35 V. Aravindan, Y.-S. Lee, R. Yazami and S. Madhavi, *Mater. Today*, 2015, **18**, 345–351.

36 Y. Devrim and A. Albostan, *J. Electron. Mater.*, 2016, **45**, 3900–3907.

37 G. Zhang, M. Wen, S. Wang, J. Chen and J. Wang, *RSC Adv.*, 2018, **8**, 567–579.

38 T. Ohsaka, F. Izumi and Y. Fujiki, *J. Raman Spectrosc.*, 1978, **7**, 321–324.

39 W. F. Zhang, Y. L. He, M. S. Zhang, Z. Yin and Q. Chen, *J. Phys. D: Appl. Phys.*, 2000, **33**, 912–916.

40 A. C. Ferrari, *Solid State Commun.*, 2007, **143**, 47–57.

41 N. Dubouis, P. Lemaire, B. Mirvaux, E. Salager, M. Deschamps and A. Grimaud, *Energy Environ. Sci.*, 2018, **11**, 3491–3499.

42 V. J. Ovejas and A. Cuadras, *Batteries*, 2018, **4**, 43.

43 A. Barai, K. Uddin, W. D. Widanage, A. McGordon and P. Jennings, *Sci. Rep.*, 2018, **8**, 1–13.

44 J. G. Zhu, Z. C. Sun, X. Z. Wei and H. F. Dai, *RSC Adv.*, 2014, **4**, 29988–29998.

45 H. Dai, B. Jiang and X. Wei, *Energies*, 2018, **11**, 220.